

THE IMPACT OF GALAXY FORMATION ON THE SUNYAEV-ZELDOVICH EFFECT OF GALAXY CLUSTERS

DAISUKE NAGAI

Department of Astronomy and Astrophysics,
Kavli Institute for Cosmological Physics,
5640 S. Ellis Ave., The University of Chicago, Chicago IL 60637
e-mail: daisuke@oddjob.uchicago.edu

Draft version October 1, 2018

ABSTRACT

We study the effects of galaxy formation on the Sunyaev-Zel'dovich effect (SZE) observable-mass relations using high-resolution cosmological simulations. The simulations of eleven individual clusters spanning a decade in mass are performed with the shock-capturing Eulerian adaptive mesh refinement N-body+gasdynamics ART code. To assess the impact of galaxy formation, we compare two sets of simulations performed in an adiabatic regime (without galaxy formation) and those with several physical processes critical to various aspects of galaxy formation: radiative cooling, star formation, stellar feedback and metal enrichment. We show that a SZE signal integrated to a sufficiently large fraction of cluster volume correlates strongly with its enclosed mass, independent of details of gas physics and dynamical state of the cluster. The slope and redshift evolution of the SZE flux-mass relation are also insensitive to processes of galaxy formation and are well characterized by a simple self-similar cluster model. Its normalization, on the other hand, is significantly affected by gas cooling and associated star formation. Our simulations show that inclusion of these processes suppresses the normalization by $\approx 30 - 40\%$. The effect is due to a decrease in gas mass fraction, which is offset slightly by an increase in gas mass-weighted temperature. Gas cooling and star formation also cause an increase in total mass and modify the normalization by a few percent. Finally, we compare the results of our simulations to recent observations of the SZE scaling relations obtained using 36 OVRO/BIMA SZE+*Chandra* X-ray observations. The comparison highlights the importance of galaxy formation in theoretical modelling of clusters and shows that current generation of simulations produce clusters with gross properties quite similar to their observed counterparts.

Subject headings: cosmology: theory—clusters: formation— methods: numerical

1. INTRODUCTION

The Sunyaev-Zel'dovich effect (SZE) is a potentially powerful observational tool for cosmology. It is a small distortion in the cosmic microwave background (CMB) spectrum caused by scattering of CMB photons off a distribution of high energy electrons in dense structures such as clusters of galaxies (Sunyaev & Zeldovich 1970, 1972). This effect has the unique property that its signal is independent of redshift, making it particularly well suited for deep cluster surveys (e.g., Holder et al. 2000; Weller et al. 2002). The next generation of SZE instruments, such as the South Pole Telescope (SPT) and the Atacama Cosmology Telescope (ACT), should be capable of mapping a fairly large portion of the sky and finding a large number ($\gtrsim 10^4$) of clusters out to high-redshift. Such large and homogeneous sample of galaxy clusters will enable direct and precise measurements of their number density as a function of redshift, and the expected survey yields will be sufficient to provide one of the most powerful constraints on the nature of dark energy (Wang & Steinhardt 1998; Haiman et al. 2001).

To realize the full statistical power of the upcoming SZE surveys, however, systematic uncertainties would have to be controlled at a level comparable to statistical uncertainties. One of the main sources of the systematic uncertainties lie in the relation between the SZE observable and cluster mass as a function of redshift. Making this connection is important because the cluster mass is

not directly observable. For the future SZE surveys, the requirement is to control systematic uncertainties in the SZE observable-mass relations to better than $\sim 5\%$ at all redshift (e.g., Carlstrom et al. 2002).

This poses a serious challenge to both observers and theorists. To date, observational studies of the SZE scaling relations have been performed using two largest datasets of SZE measurements obtained by the OVRO/BIMA cm-wave imaging experiment (Cooray 1999; McCarthy et al. 2003; LaRoque 2005) and multi-band SuZIE experiment (Benson et al. 2004) along with X-ray observations. Analyzing a sample of 36 clusters observed with both the OVRO/BIMA SZE imaging and *Chandra* X-ray observations, LaRoque (2005) showed that there are tight correlations between the observed SZE flux and X-ray temperature and cluster masses. The observed regularity of the SZE effect of clusters is encouraging news, but further progress is clearly needed for the future SZE surveys. The observational situation is expected to improve rapidly with the advent of a number of dedicated SZE survey instruments, which will dramatically increase the sample size and the number of low-mass clusters.

On a theoretical side, a number of groups have studied the SZE scaling relations using semi-analytic models (Verde et al. 2002; McCarthy et al. 2003) and cosmological simulations (Metzler 1998; White et al. 2002; da Silva et al. 2004; Diaferio et al. 2005; Motl et al. 2005). Motivated by results of X-ray observations in a

past decade (see Voit 2005, for a review and references therein), recent studies have focused on studying the effects of non-gravitational physical processes, including gas cooling, star formation and energy feedback, on the SZE scaling relations. One of the main results is that a SZE signal integrated to a sufficiently large fraction of cluster volume is an extremely good proxy for its enclosed mass, independent of details of gas physics and dynamical state of a cluster (see e.g., Motl et al. 2005). The slope and the redshift evolution of the SZE scaling relation also appear to be insensitive to details of cluster gas physics (e.g., da Silva et al. 2004). While these results are encouraging for cosmological applications, these previous studies have focused on simulating a large number of clusters, and the resolution was inevitably limited to capture relevant cluster physics. As such, the impact of galaxy formation on normalization of the SZE scaling relations has not yet converged among different simulations. It is therefore important to push theoretical modelling of SZE scaling relations and check previous results using higher-resolution cluster simulations.

In this paper, we present such study using high-resolution cosmological simulations of cluster formation. Although the statistic is limited, our cluster sample spans over a decade in mass and provide a good leverage on scaling relations. The mass resolution of our simulations is more than an order of magnitude higher than that in previous studies. This work is therefore complimentary to the previous studies in a literature. Using these simulations, we study the impact of gas cooling and star formation on the SZE scaling relations, including their normalization, slope and redshift evolution. To test the results of our simulations, we compare our results to recent observations of the SZE scaling relations based on a sample of 36 clusters obtained using the OVRO+BIMA SZE and *Chandra* X-ray telescopes (LaRoque 2005).

The paper is organized as follows. In § 2 we define observational quantities and present relevant scaling laws predicted by a self-similar cluster model. We describe simulations presented in this paper in § 3 and present results and comparisons to previous studies and recent observational results in § 4. Finally, in § 5 we discuss our conclusions and their implications for SZE cluster surveys.

2. THEORETICAL FRAMEWORK

2.1. Thermal Sunyaev-Zel'dovich Effect

The thermal SZE is a distortion in the CMB spectrum produced by the inverse Compton scattering of CMB photons off free electrons in dense structures such as clusters of galaxies. For a given line of sight, a change in the CMB specific intensity caused by the thermal SZE at a frequency ν is given by $\Delta I_\nu / I_{\text{CMB}} = f_\nu(x) g_\nu(x) y$. The dimensionless Comptonization parameter y is defined as,

$$y \equiv \frac{k_B \sigma_T}{m_e c^2} \int n_e(l) T_e(l) dl. \quad (1)$$

where n_e and T_e are the number density and temperature of electrons, m_e is the electron rest mass, c is the speed of light, and σ_T is the Thomson cross-section. There are several frequency dependent factors, including $I_{\text{CMB}} = 2h\nu^3/c^2(e^x - 1)^{-1}$, $f_\nu(x) = [x(e^x + 1)/(e^x - 1) - 4](1 + \delta_{\text{SZE}}(x, T_e))$ and $g_\nu(x) = x^4 e^x / (e^x - 1)^2$, where

$\delta_{\text{SZE}}(x, T_e)$ is the frequency dependent relativistic correction and $x \equiv h\nu/k_B T_{\text{CMB}}$. The corresponding change in the CMB temperature is given by $\Delta T_\nu / T_{\text{CMB}} = f_\nu(x) y$. In the Rayleigh-Jeans limit ($\nu \ll 200\text{GHz}$), $\Delta T_\nu / T_{\text{CMB}} = -2y$ and $\Delta I_\nu = (2k_B \nu^2 / c^2) \Delta T_\nu$.

Let us now consider the SZE signal arising from a cluster located at redshift z . The SZE flux integrated over a solid angle of observation $d\Omega$ is given by $\Delta S_\nu = \int \Delta I_\nu d\Omega = I_{\text{CMB}} f_\nu(x) g_\nu(x) Y$, where Y is the integrated Compton- y parameter defined as

$$Y \equiv \int_\Omega y d\Omega = \frac{1}{d_A^2(z)} \left(\frac{k_B \sigma_T}{m_e c^2} \right) \int_V n_e T_e dV, \quad (2)$$

and $d\Omega = dA/d_A^2(z)$ is the solid angle of the cluster subtended on the sky, $d_A(z)$ is the angular diameter distance to the cluster, dA is the area of the cluster on the sky, and dV is the cluster volume. Because Y depends on a distance, we will work with the intrinsic thermal SZE signal, defined as

$$Y^{\text{int}} \equiv Y d_A^2(z) \propto f_{\text{gas}} M T_m. \quad (3)$$

Note that the integrated SZE flux is linearly sensitive to gas mass $M_{\text{gas}} = f_{\text{gas}} M$ and mass-weighted temperature T_m , where f_{gas} is the gas mass fraction and M is the total cluster mass.

2.2. Self-Similar scaling relations

In the absence of cooling and heating processes, clusters are expected to scale self-similarly (Kaiser 1986). The self-similar model predicts that the temperature of the gas scales with the cluster mass as

$$M \propto T^{3/2} E^{-1}(z) \quad (4)$$

where $M \equiv 4\pi r_\Delta^3 \Delta_c \rho_{\text{crit}} / 3$ is a halo mass enclosed within r_Δ , defined as a radius of spherical volume within which the mean density is Δ_c times the *critical density*, ρ_{crit} , at that redshift (Bryan & Norman 1998). $E(z)$ is the redshift-dependent Hubble parameter, defined as $H(z) = 100hE(z) \text{ km s}^{-1} \text{ Mpc}^{-1}$, and it is given by $E^2(z) = \Omega_M(1+z)^3 + \Omega_\Lambda$ for a flat cosmology.

Inserting Eq. 4 into Eq. 3, we obtain SZE scaling relations predicted by the self-similar model,

$$Y^{\text{int}} \propto \begin{cases} f_{\text{gas}} M^{5/3} E^{2/3}(z) \\ f_{\text{gas}} T^{5/2} E^{-1}(z) \end{cases} \quad (5)$$

3. SIMULATIONS

In this study, we analyze high-resolution cosmological simulations of eleven cluster-size systems in the ‘‘concordance’’ flat Λ CDM model with $\Omega_m = 1 - \Omega_\Lambda = 0.3$, $\Omega_b = 0.04286$, $h = 0.7$ and $\sigma_8 = 0.9$, where the Hubble constant is defined as $100h \text{ km s}^{-1} \text{ Mpc}^{-1}$, and σ_8 is the power spectrum normalization on $8h^{-1} \text{ Mpc}$ scale. The simulations were done with the Adaptive Refinement Tree (ART) N -body+gasdynamics code (Kravtsov 1999; Kravtsov et al. 2002), an Eulerian code that uses adaptive refinement in space and time, and (non-adaptive) refinement in mass (Klypin et al. 2001) to reach the high dynamic range required to resolve galaxy-size halos formed in self-consistent cosmological cluster simulations.

To set up initial conditions we first ran a low resolution simulation of $80h^{-1} \text{ Mpc}$ and $120h^{-1} \text{ Mpc}$ boxes

and selected eleven clusters with mass ranging from $M_{500c} \approx 3.5 \times 10^{13}$ to $9 \times 10^{14} h^{-1} M_{\odot}$. Table 1 lists properties of clusters at the present epoch. The perturbation modes in the Lagrangian region corresponding to a sphere of several virial radii around each cluster at $z=0$ was then re-sampled at the initial redshift of $z_i = 25$ for three most massive clusters (CL1-3) and $z_i = 49$ for remaining eight clusters in the sample. For the three most massive clusters we have resampled radius of $3R_{\text{vir}}(z=0)$, while for the rest of the clusters the resampling sphere had radius of $5R_{\text{vir}}(z=0)$, where $R_{\text{vir}}(z=0)$ is the virial radius enclosing overdensities of $\Delta_{\text{vir}} = 334$ with respect to the mean density of the universe at $z=0$. During the resampling we retained previous large-scale waves intact but included additional small-scale waves, as described by Klypin et al. (2001). The resampled Lagrangian region of each cluster was then re-simulated with high dynamic range.

High-resolution simulations were run using 128^3 uniform grid and 8 levels of mesh refinement in computational boxes of $120h^{-1}$ Mpc for CL1-CL3 and $80h^{-1}$ Mpc for CL4-CL11, which corresponds to the dynamic range of $128 \times 2^8 = 32768$ and the peak formal resolution of $80/32,768 \approx 2.44h^{-1}$ kpc, corresponding to the actual resolution of $\approx 2 \times 2.44 \approx 5h^{-1}$ kpc. Only the region of $\sim 3 - 10h^{-1}$ Mpc around a cluster was adaptively refined, the rest of the volume was followed on the uniform 128^3 grid. The mass resolution corresponds to the effective 512^3 particles in the entire box with a particle mass $m_p = 1.07 \times 10^9 M_{\odot}$ and $3.16 \times 10^8 M_{\odot}$, or the Nyquist wavelength of $\lambda_{\text{Ny}} = 0.469h^{-1}$ and $0.312h^{-1}$ comoving megaparsec for CL1-3 and CL4-11, respectively, or $0.018h^{-1}$ and $0.006h^{-1}$ Mpc in physical units at initial redshift of the simulations. The dark matter particle mass in the region around the cluster is therefore $(1 - f_b)m_p = 9.1 \times 10^8 h^{-1} M_{\odot}$ for CL1-3 and $2.7 \times 10^8 h^{-1} M_{\odot}$ for CL4-CL11 (where $f_b = \Omega_b/\Omega_m = 0.1429$), while other regions were simulated with lower mass resolution.

As the zeroth-level fixed grid consisted of only 128^3 cells, we started the simulation already pre-refined to the 2nd level ($l = 0, 1, 2$) in the high-resolution Lagrangian regions of clusters. This is done to ensure that the cell size is equal to the mean interparticle separation and all fluctuations present in the initial conditions are evolved properly. During the simulation, refinements were allowed to the maximum $l = 8$ level and refinement criteria were based on the local mass of DM and gas in each cell. The logic is to keep the mass per cell approximately constant so that the refinements are introduced to follow collapse of matter in a quasi-Lagrangian fashion. For the DM, we refine the cell if it contains more than two dark matter particles of the highest mass resolution specie. For gas, we allow the mesh refinement, if the cell contains gas mass larger than four times DM particle mass scaled by the baryon fraction. In other words, the mesh is refined if the cell contains DM mass larger than $2(1 - f_b)m_p$ or gas mass larger than $= 4f_b m_p$. We analyze clusters at the present-day epoch as well as their progenitors at higher redshifts.

We repeated each cluster simulation with and without radiative cooling and star formation. The first set of “adiabatic” simulations have included only the stan-

dard gasdynamics for the baryonic component without radiative cooling and star formation. The second set of simulations included gasdynamics and several physical processes critical to various aspects of galaxy formation: radiative cooling, star formation, metal enrichment and thermal feedback due to the supernovae type II and type Ia, self-consistent advection of metals, metallicity dependent radiative cooling and UV heating due to cosmological ionizing background (Haardt & Madau 1996). We will use labels ‘AD’ and ‘CSF’ for the adiabatic simulations and the simulations with gas cooling and star formation, respectively.

Cooling and heating rates take into account Compton heating and cooling of plasma, UV heating, atomic and molecular cooling and are tabulated for the temperature range $10^2 < T < 10^9$ K and a grid of metallicities, and UV intensities using the `Cloudy` code (ver. 96b4, Ferland et al. 1998). The `Cloudy` cooling and heating rates take into account metallicity of the gas, which is calculated self-consistently in the simulation, so that the local cooling rates depend on the local metallicity of the gas. Star formation in these simulations was done using an observationally-motivated recipe (e.g., Kennicutt 1998): $\dot{\rho}_* = \rho_{\text{gas}}^{1.5}/t_*$, with $t_* = 4 \times 10^9$ yrs. The detailed description and implementation of the star formation are provided in Kravtsov et al. (2005).

The code also accounts for the stellar feedback on the surrounding gas, including injection of energy and heavy elements (metals) via stellar winds and supernovae and secular mass loss. Once formed, each stellar particle is treated as a single-age stellar population and its feedback on the surrounding gas is implemented accordingly. More specifically, in the simulations analyzed here, we assumed that a stellar initial mass function (IMF) is described by the Miller & Scalo (1979) functional form with stellar masses in the range $0.1 - 100 M_{\odot}$. All stars more massive than $M_* > 8 M_{\odot}$ deposit 2×10^{51} ergs of thermal energy in their parent cell¹ and a fraction $f_Z = \min(0.2, 0.01M_* - 0.06)$ of their mass as metals, which crudely approximates the results of Woosley & Weaver (1995). In addition, stellar particles return a fraction of their mass and metals to the surrounding gas at a secular rate $\dot{m}_{\text{loss}} = m_* C_0(t - t_{\text{birth}} + T_0)^{-1}$ with $C_0 = 0.05$ and $T_0 = 5$ Myr (Jungwiert et al. 2001). The code also accounts for the SNIa feedback assuming a rate that slowly increases with time and broadly peaks at the population age of 1 Gyr. We assume that a fraction of 1.5×10^{-2} of mass in stars between 3 and $8 M_{\odot}$ explodes as SNIa over the entire population history and each SNIa dumps 2×10^{51} ergs of thermal energy and ejects $1.3 M_{\odot}$ of metals into the parent cell. For the assumed IMF, 75 SNII (instantly) and 11 SNIa (over several billion years) are produced by a $10^4 M_{\odot}$ stellar particle.

High-resolution² and inclusion of various physical processes are critical for assessing the effects of galaxy formation on properties and evolution of the ICM. For example, Kravtsov et al. (2005) showed that gas cooling and star formation significantly suppress gas mass fractions

¹ No delay of cooling was introduced in these cells after SN energy release.

² The mass and spatial resolution are high enough to resolve galactic-size halos whose mass is as small as 10^{-4} of the host cluster mass (Nagai & Kravtsov 2005).

TABLE 1
SIMULATED CLUSTER SAMPLE OF THE CSF RUN AT $z=0$

Name	R_{500c} $h^{-1}\text{Mpc}$	M_{500c}^{gas} $h^{-1}10^{13}M_{\odot}$	M_{500c}^{tot} $h^{-1}10^{14}M_{\odot}$	$\langle T_{\text{spec}} \rangle$ keV
CL1	1.160	8.19	9.08	10.0
CL2	0.976	5.17	5.39	8.1
CL3	0.711	1.92	2.09	4.1
CL4	0.609	1.06	1.31	2.7
CL5	0.661	1.38	1.68	3.9
CL6	0.624	1.22	1.41	3.2
CL7	0.522	0.74	0.82	1.7
CL8	0.487	0.43	0.67	2.2
CL9	0.537	0.78	0.90	2.2
CL10	0.509	0.62	0.77	2.1
CL11	0.391	0.27	0.35	1.2

in clusters. Interestingly, the results of numerical simulations agree quite well with recent X-ray and SZE measurements (e.g., LaRoque et al. 2006, Kravtsov et al., in preparation). Note also that the level of entropy and metal abundance in these simulations also compare well with recent X-ray observations. Because the SZE signal depends linearly on the gas mass fraction, these results indicate that the impact of galaxy formation on the SZE flux may also be significant.

Throughout this paper we use estimates of Y^{int} , mass and other cluster observables within different commonly used radii, defined by the total matter overdensity they enclose. We will use radii r_{2500} , r_{500} , r_{200} enclosing overdensities of $\Delta_c = 2500$, 500, and 200 with respect to the critical density, ρ_{crit} , as well as radii r_{180} and r_{vir} enclosing overdensities of $\Delta_m = 180$ and Δ_{vir} with respect to the mean density of the universe. The latter is equal to $\Delta_{\text{vir}} \approx 334$ at $z=0$ and ≈ 200 at $z=1$ for the cosmology adopted in our simulations. The virial radius and masses of clusters within r_{500c} for the CSF run at $z=0$ are given in Table 1. For reference, we also give a spectral X-ray temperature, $\langle T_{\text{spec}} \rangle$, of individual clusters extracted from mock *Chandra* analysis (Nagai, Vikhlinin & Kravtsov 2006, in preparation), and it is equivalent to a single-temperature fit to the cluster spectrum extracted from the radial range $0.15 < r/r_{500c} < 1.0$.

4. RESULTS

In this section, we study the impact of galaxy formation on the SZE scaling relations using cosmological simulations of cluster formation. Our general strategy is to assess their effects on cluster observables and scaling relations by comparing two sets of simulations with and without processes important for galaxy formation.

4.1. Pressure Profiles

Since the thermal SZE is sensitive to the pressure of the ICM, we will start with the analysis of pressure profiles of clusters. Figure 1 shows a comparison of the mean pressure profiles of clusters simulated in the adiabatic regime and those with gas cooling and star formation at $z=0$ and

$z=1$. To compute the mean profiles, we first normalize differential and cumulative pressure profiles of individual clusters using the mean integrated pressure within a sphere of r_{500c} , denoted as \bar{P}_{500c} , and plot them as a function of the cluster-centric radius in units of r_{500c} . The mean profiles are computed by averaging the normalized profiles over the entire cluster sample. To highlight the impact of gas cooling and star formation on the pressure profiles, we normalize the pressure profile of the CSF run using \bar{P}_{500c} of the AD run for each cluster. The shaded bands show 1σ rms scatter around the mean profile of the CSF runs. The mean and scatter of the profiles are computed for a logarithm of pressure.

Fig. 1 illustrates that clusters ranging in an order of magnitude in mass exhibit remarkably similar pressure profiles at all radii. The differential pressure profile declines by nearly four orders of magnitude from the center to r_{500c} , and the scatter is small ($\approx 20\%$) throughout clusters. In the outskirts, the radial profile of gas pressure generally falls faster than that of gas or dark matter density. This is because pressure is a product of gas density and gas mass-weighted temperature for the ideal gas, and the latter also declines with radius (see Motl et al. 2005; Vikhlinin et al. 2005). For example, a typical power-law slope of the differential pressure profile is ≈ -3.5 at r_{500c} , which is steeper than a typical slope of the density profile of ≈ -3 seen in cosmological simulations (Navarro et al. 1996, 1997) as well as recent X-ray observations (Vikhlinin et al. 2006).

One of the main results from this analysis is that gas pressure is suppressed in a region outside $r \gtrsim 0.1r_{500c}$ in the CSF runs compared to the AD runs. The cumulative pressure at r_{500c} , for example, is suppressed by $\approx 25\%$ on average, and this effect is relatively constant ($\approx 25 - 35\%$) in a region outside $> 0.2r_{500c}$ at $z=0$. In the center, gas pressure is significantly more concentrated, because of strong gas cooling and contraction of dark matter (Gnedin et al. 2004). Note, however, that this high pressured cluster core contributes very little to the cumulative pressure at large radii. For example, the inner regions within $< 0.1r_{500c}$ contribute less than 2% of the total SZE signal within r_{500c} . Thus, the SZE signal integrated out to a sufficiently large radius is insensitive to properties of cluster cores.

Although general trends are similar, the suppression of gas pressure varies more strongly with radius at $z=1$, because a dense, cool core dominates a larger fraction of r_{500c} at high redshift. Nevertheless, we find that the suppression of the cumulative pressure at r_{500c} is comparable at $z=0$ and 1. However, the difference becomes more apparent in the inner region; for example, the effect at r_{2500c} changes from 35% at $z=0$ to 20% at $z=1$. If a similar trend exists in real clusters this implies that redshift evolution of the SZE scaling relations is expected to deviate from the prediction of the self-similar model, if the SZE flux is computed within the aperture considerably smaller than r_{500c} .

In order to better understand the suppression of gas pressure, we examine the impact of gas cooling and star formation on density, temperature and entropy profiles of the ICM. Figure 2 shows that the suppression of pressure is accompanied by strong suppression in gas density and moderate increase in gas mass-weighted temperature. An entropy profile provides further insights into

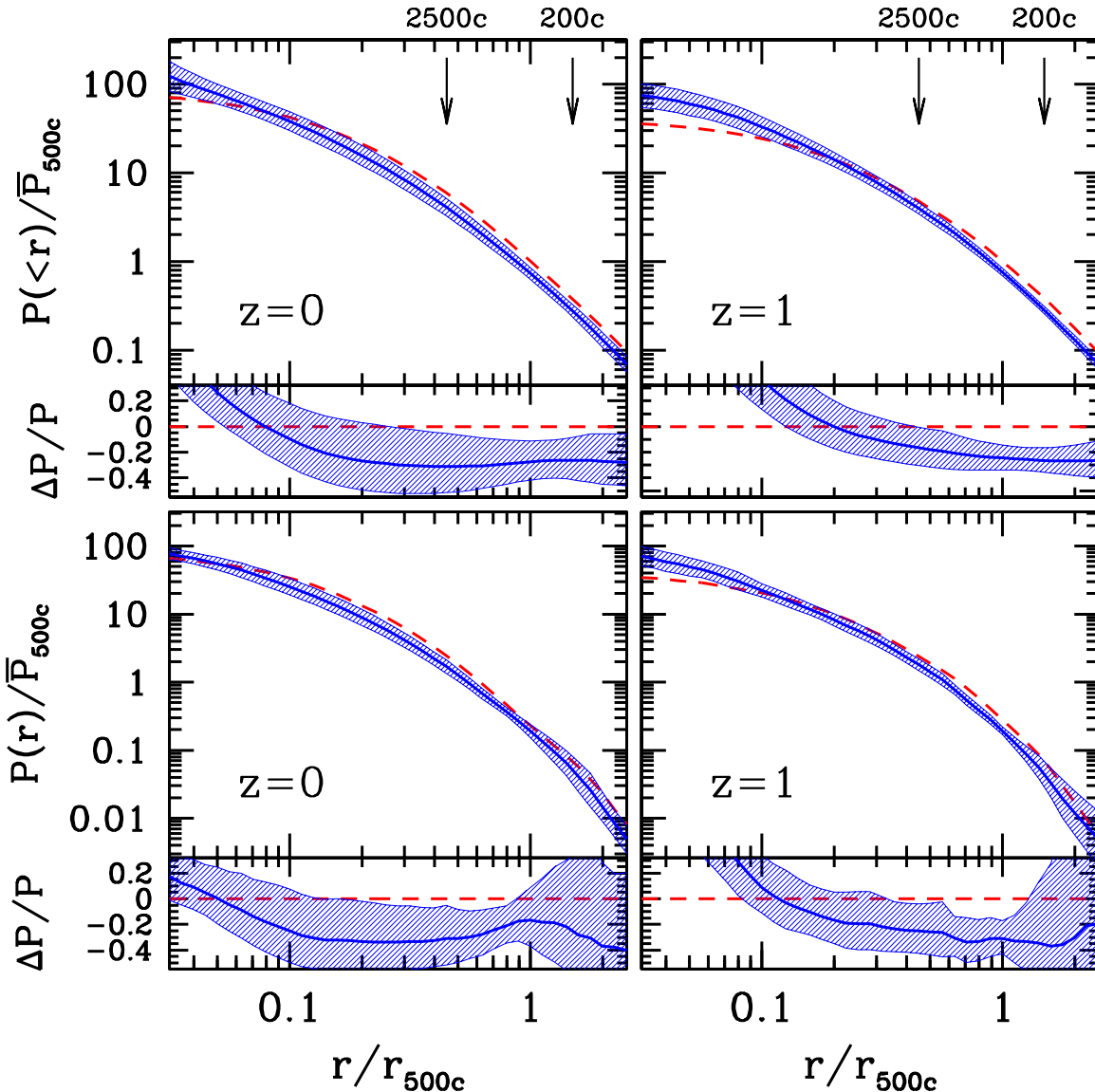


FIG. 1.— Cumulative (*top panels*) and differential (*bottom panels*) pressure profiles for the eleven clusters used in our analysis at $z=0$ (*left column*) and $z=1$ (*right column*). The *dashed* and *solid* lines show mean profiles in the AD and CSF simulations averaged over all clusters, respectively. Note that all profiles are normalized to the mean cumulative pressure at r_{500c} in the AD runs, \bar{P}_{500c} , at each epoch. The *bottom panel* of each figure shows the fractional deviation of the mean profile of the CSF run relative to the mean profile of the AD run. In all panels, the *shaded* bands indicate 1σ rms scatter around the mean. The vertical arrows in the top panels indicate the radii enclosing overdensities of 2500 and 200 with respect to the critical density at each epoch.

these phenomena, because it uniquely characterizes thermodynamic properties of the ICM, given a shape of its confining potential well (see Voit et al. 2002 and references therein). Fig. 2 shows that the entropy of the ICM, defined as $S \equiv T/n_e^{2/3}$, is enhanced from $0.05 \times r_{500c}$ out to $2 \times r_{500c}$. The effect peaks around $0.3r_{500c}$, and the entropy is enhanced by about 40% at r_{500c} . In our simulations, gas cooling and star formation can increase the entropy of the gas in one of two ways: (1) the level of entropy is elevated throughout as gas cooling and star formation proceed in the cluster center (Voit & Bryan 2001)³ or (2) direct heating of the ICM by energy in-

³ Gas cooling and star formation remove low entropy gas and

jection from supernova explosions. The former is likely a dominant mechanism that shapes the overall entropy distribution, while the second process is important for regulating a rate of gas cooling in high density regions (e.g., a vicinity of a central galaxy and cluster galaxies), where stars are forming with sufficiently high rates.

To examine a mass dependence of the effects, we split the sample in half and show the mean profiles of six most massive ($T_X \gtrsim 2\text{keV}$) and five least massive ($T_X \lesssim 2\text{keV}$)

cause an inflow of high entropy gas from outside to maintain the stability of the cluster core. In this way, the low-entropy gas in the inner region is gradually replenished with the high-entropy gas flowing in from outside, and the level of entropy is gradually elevated throughout the cluster as gas cooling and star formation proceed in the cluster core.

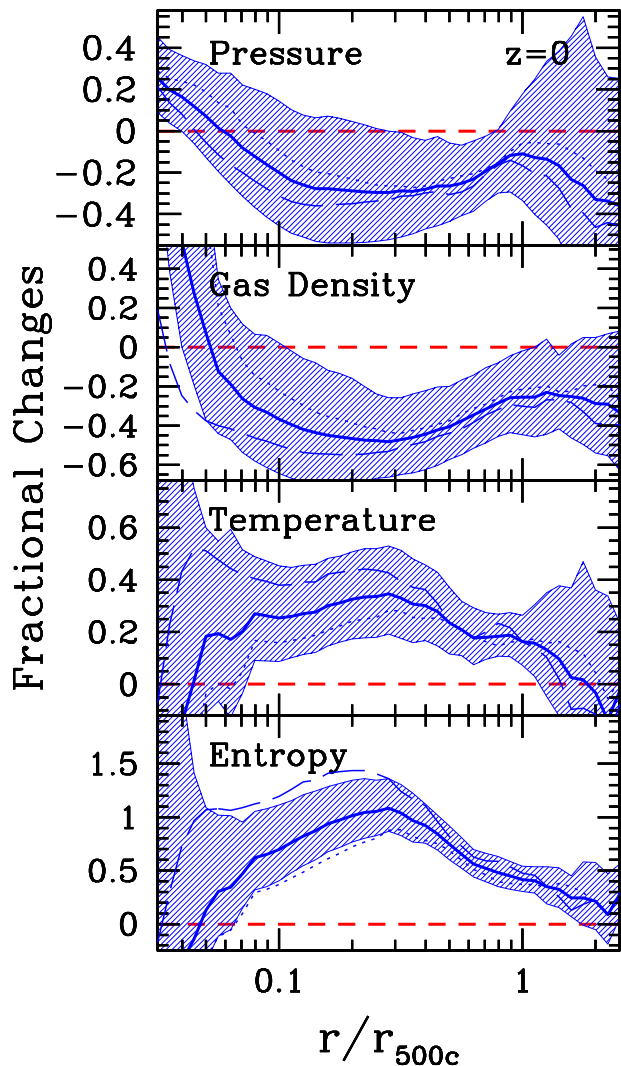


FIG. 2.— The impact of galaxy formation on pressure, gas density, temperature and entropy profiles (*from top to bottom*) of the simulated clusters at $z=0$. The *solid* lines show fractional changes in the mean differential radial profiles in the CSF runs averaged over eleven clusters relative to the mean profiles in the AD runs, indicated by lines at zero. The *dotted* and *dashed* lines show the same for subsamples of six most and five least massive clusters, respectively. Note that the mean profile of each quantity is computed by first normalizing a profile of each cluster by the value of the cumulative profile at r_{500c} and averaging the normalized profile over all clusters.

clusters in Fig. 2. Note that the former includes clusters dominated by bremsstrahlung or those that are about equal in the importance of bremsstrahlung and line cooling, while the latter includes clusters dominated by line emission. Fig. 2 shows that a shape and normalization of the pressure profiles exhibit the smallest systematic trend with mass. In the outskirts ($r > 0.3r_{500c}$) of the clusters, there is a similarly small systematic trend with mass for gas density, temperature and entropy profiles. In the inner regions, on the other hand, we find a slightly more pronounced mass dependence in all profiles. Among them, the pressure profiles show the smallest trend with mass. In less massive clusters, changes in gas density and temperature become larger but with op-

posite signs; therefore, these effects cancel each other to give the smallest mass dependence on pressure. In contrast, the effects add constructively to give the largest mass dependence on entropy.

The main conclusions from the profile analysis are that gas cooling and star formation suppress the amplitude of gas pressure and therefore the SZE signal, and the magnitude of the effects depends rather weakly on the cluster mass. These results suggest that processes of galaxy formation modify normalization of the SZE flux-mass relation, but its impact on slope is expected to be small. This is a main topic of the discussion in the next section.

4.2. The SZE scaling relations

The SZE flux-total mass (SZE-M) relation is a relation most directly relevant for cosmological application. Figure 3 shows a comparison of the SZE-total mass scaling relation at r_{500c} and its redshift evolution for a sample of eleven clusters in the AD and CSF runs. At each epoch, we performed fits to the sample of simulated clusters using the simple power-law relation,

$$Y = A_{14} \times 10^{-6} \left(\frac{M}{10^{14} h^{-1} M_{\odot}} \right)^{\alpha_M}, \quad (6)$$

where A_{14} is the normalization at $10^{14} h^{-1} M_{\odot}$ in units of 10^{-6} and α_M is the slope. In practice, we fit a straight line to the $\log(Y)$ - $\log(M)$ relation by minimizing χ^2 . Table 2-4 lists the best-fit normalization and slope measured at different radii, including r_{180m} , r_{vir} , r_{200c} , r_{500c} and r_{2500c} . The values in the adiabatic simulations are marked 'ad', while those in the simulations with gas cooling and star formation are marked 'csf' (e.g., A_{14}^{csf}). The best-fit parameters in these tables and the right panel of Fig. 3 are obtained by fitting for both normalization and slope simultaneously. To highlight a deviation from the self-similar slope, the best-fit relations shown in the left panel of Fig. 3 are obtained by fixing the slope to the predicated value of 5/3. Note that fitting for the slope changes the best-fit normalization by no more than 5% at both $z=0$ and $z=1$.

In the right panel of Fig. 3, errorbars indicate 2σ confidence region of the best-fit slope and normalization in the CSF simulations at each epoch. Since the redshift evolution of normalization is measured relative to the relation at $z=0$, errorbars at $z > 0$ include uncertainties in the best-fit normalizations at each epoch and $z=0$ added in quadrature. Note also that the size of the errorbars are comparable for the AD simulations. Errorbars shown in Fig. 6 and Fig. 7 are also computed in the same way.

The left panel shows that the SZE signal integrated within a sphere of r_{500c} correlates very strongly with the enclosed cluster mass at both $z=0$ and 1. The *rms* scatter is about 10-15% in both AD and CSF runs. Moreover, we find that the slope of the AD run is in a very good agreement with the predicted slope of the self-similar model. The best-fit slope of the CSF run is also not very different from the predicted slope of 5/3, but there is an indication that the slope may be systematically steeper by $\lesssim 0.1$. Unfortunately, however, the current sample size is too small to rule out the prediction of the self-similar model with any statistical significance. A larger sample of simulated clusters is clearly needed to assess this effect in future studies.

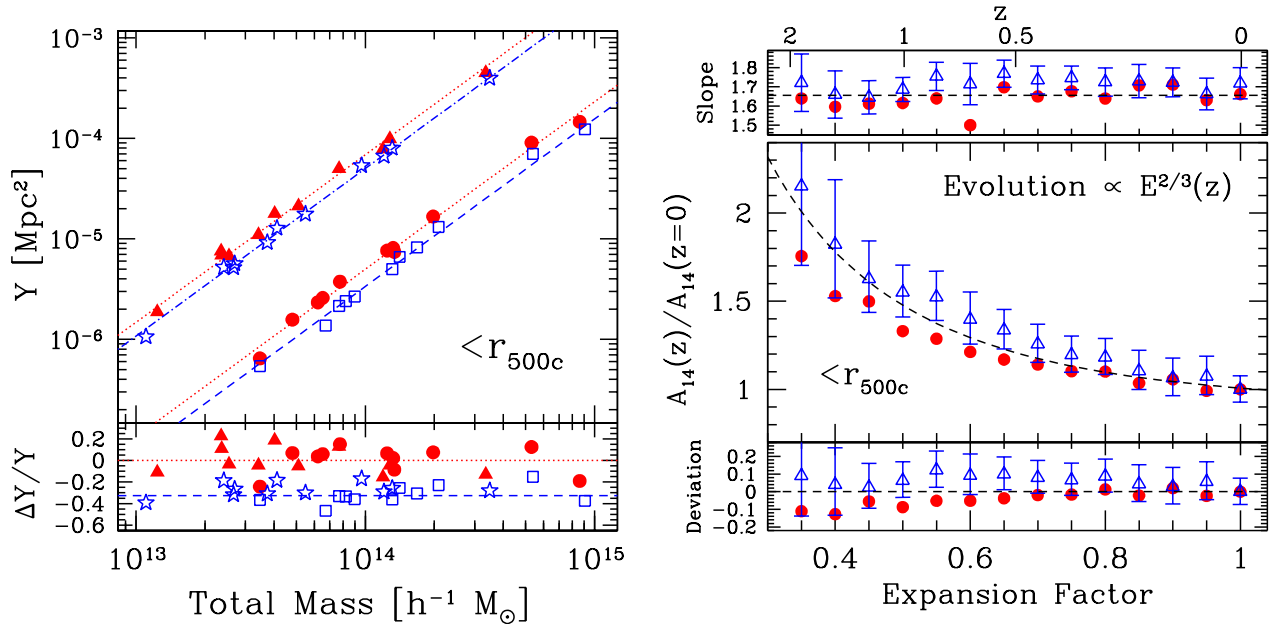


FIG. 3.— The SZE flux-total mass relations for eleven clusters in the AD (*solid symbols*) and CSF (*open symbols*) simulations. *Left-top panel*: the relation between the integrated compton- Y vs. total mass enclosed within a sphere of radius r_{500c} at $z=0$ (*bottom lines and points*) and $z=1$ (*top lines and points*). For clarity, the $z=1$ relations are shifted upward by a factor of ten. The *solid circles* and *solid triangles* indicate the AD runs at $z=0$ and 1, and the *open squares* and *open stars* are the CSF runs at $z=0$ and 1, respectively. At each epoch, the *dotted* and *dashed* lines show the best-fit relations for the AD and CSF runs with a slope fixed at the self-similar slope of $5/3$. *Left-bottom panel*: the fractional deviation of individual clusters from the best-fit relation of the AD runs at each epoch. The *dashed* line indicates the best-fit relation of the CSF runs at $z=0$. *Right panel*: the redshift evolution of slope (*top*) and normalization (*middle*) of the SZE flux-total mass relation between $z=2$ and the present day. The *solid circles* and *open squares* indicate the AD and CSF runs, respectively. The *dashed* lines indicate the slope of $5/3$ (*top*) and the evolution in normalization predicted by the self-similar model (*middle*). The errorbars indicate 2σ confidence region of the best-fit slope and normalization in the CSF runs at each epoch. The *bottom* panel shows a fractional deviation of the best-fit normalization from the self-similar prediction as a function of time.

While the tightness and slope of the relations are relatively unaffected, gas cooling and star formation significantly modify normalization of the SZE-total mass relation. Compared to the AD run, the normalization of the CSF run is lower by 41, 34 and 27% at r_{2500c} , r_{500c} and r_{180m} .

The right panel shows that the redshift evolution of the SZE-total mass relation is consistent with the predictions of the self-similar model in the entire redshift range considered here. First, the slope is constant with redshift. Second, the redshift evolution of the normalization is in a good agreement with the predicted evolution. We also find similar results at other radii considered in this paper.

To better understand the impact of galaxy formation on the SZE observable-mass relation, we also examine their effects on f_{gas} and T_m in Figure 4. Compared to the AD run, f_{gas} is lower by 38% in the CSF run; however, its effect on the SZE flux is offset partially by an increase in T_m by 9%. The net effect is a reduction of the SZE signal by 32%, which falls slightly short of a 34% change in the normalization of the SZE- M relation. This illustrates that changes in f_{gas} and T_m alone do not fully account for the change in normalization.

In addition, gas cooling and star formation slightly modify the total cluster mass. Figure 5 illustrates that inclusion of these processes cause an increase in M_{tot} at r_{500c} by about 6% on average. The effect becomes larger at a smaller radii, and it is about 10% at r_{2500c} . This

effect causes shifts in the SZE- M relation in both x- and y-directions by the same amount. However, since the slope of the relation is $\approx 5/3$, the 6% shift in the positive x-axis translates into a 8% shift in the negative y-axis. The net effect is therefore a negative 3% change in normalization due to the change in M_{tot} . Putting them all together, we find that the 34% decrease in normalization of the SZE- M relation at r_{500c} is due to combined effects of the 38% decrease in f_{gas} , the 9% increase in T_m and the net 3% decrease in normalization due to the change in M_{tot} . Note also that inclusion of gas cooling and star formation lowers the integrated SZE signal (Y^{int}) and the gas mass (M_g) within r_{500c} by 29% and 35%, respectively.

Finally, we check the redshift evolution of f_{gas} and T_m . The self-similar model predicts that f_{gas} is constant with time, while T_m of a given cluster mass evolves with time according to Eq. 4. To examine deviations from the predicted evolution, Figure 6 plots the deviations of the best-fit normalization of the $f_{gas} - M$ and the $T_m - M$ relations at $M_{500c} = 10^{14} h^{-1} M_\odot$ from the self-similar prediction as a function of redshift for the AD and CSF runs. Fig. 6 shows that f_{gas} of a given mass in the AD runs is consistent with the predicted evolution of the self-similar model, while gas cooling and star formation cause deviations, which increase toward higher redshifts. In the CSF runs, f_{gas} is higher by about 12% at $z=1$ and 17% at $z=2$ compared to their values at $z=0$. T_m , on the other hand, is lower by an almost equal amount at higher

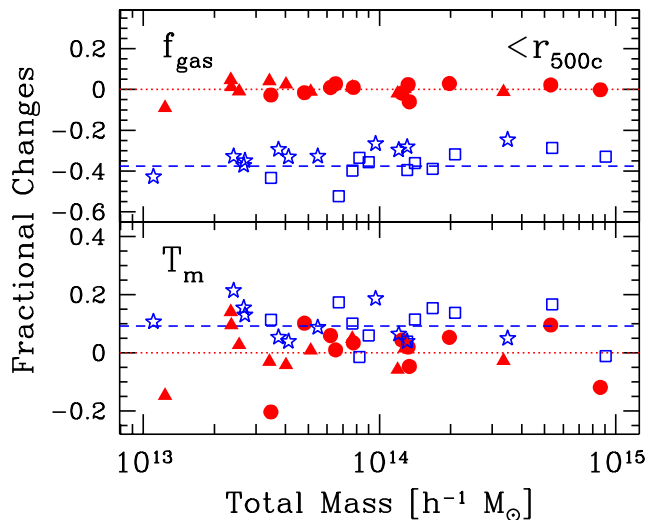


FIG. 4.— Fractional changes in gas mass fraction (*top*) and mass-weighted temperature (*bottom*) enclosed within a sphere of radius r_{500c} between the AD and CSF simulations as a function of cluster mass. The *solid circles* and *solid triangles* are the AD runs at $z=0$ and 1, and the *open squares* and *open stars* are the CSF runs at these epochs, respectively. The *dashed* line indicates a mean fractional change in f_{gas} or T_m in the CSF run at $z=0$ compared to that of the AD run, indicated by the *dotted* line at zero.

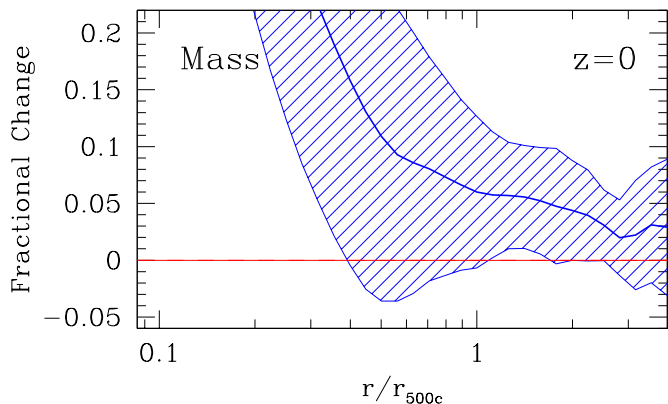


FIG. 5.— Effects of gas cooling and star formation on total mass profiles of simulated clusters at $z=0$. The *solid* line shows a change in the total mass profiles in the CSF simulations compared to that in the AD simulations averaged over *ten* clusters. For each cluster, we compute a fractional change in the total mass profiles of the CSF and AD runs, $(M_{CSF} - M_A)/M_A$, at the same physical radius, where M_{CSF} and M_A are the total mass profiles of the CSF and AD runs. We then plot the fractional change between two runs as a function of radius in units of r_{500c} and average over ten clusters, while excluding one cluster experiencing a major merger at $z=0$.

redshifts in both the AD and CSF runs. Since the SZE signal is linearly proportional to both of these quantities, the evolution in f_{gas} is canceled almost exactly by the evolution in T_m . Note also that we did not find any systematic evolution in the impact of gas cooling and star formation on the total mass with redshift. This explains why the SZE signal of a given mass shows very little evo-

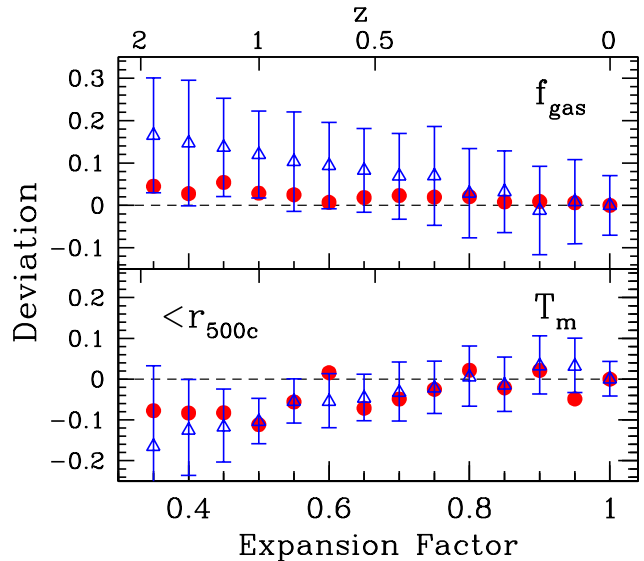


FIG. 6.— The evolution of gas mass fraction (*top*) and mass-weighted temperature (*bottom*) at $M_{500c} = 10^{14} h^{-1} M_\odot$. The fractional deviation of the best-fit normalization from the self-similar prediction, indicated by the *dashed* line. The errorbars indicate 2σ statistical uncertainties in the CSF runs at each epoch.

lution beyond the evolution predicted by the self-similar model.

So far, we have focused on the SZE-total mass relation because of its direct relevance for cosmological studies. Unfortunately, however, the cluster mass is not directly observable, and making unbiased measurements of the SZE-M relation is difficult in practice. Therefore, it is also useful to study relations between the SZE signal and cluster properties that can be measured more reliably from observations, as they can provide useful direct tests of simulations.

Here, we consider two such quantities: gas mass (M_g) and mass-weighted temperature (T_m) of clusters. Figure 7 shows SZE- M_g and SZE- T_m relations at r_{500c} and evolution of their slope and normalization with redshift. At each timestep, we perform a fit to the entire sample of simulated clusters using the following simple power-law relations,

$$Y = A_{13} \times 10^{-6} \left(\frac{M_g}{10^{13} h^{-1} M_\odot} \right)^{\alpha_{M_g}} \quad (7)$$

$$Y = A_5 \times 10^{-5} \left(\frac{T_m}{5 \text{ keV}} \right)^{\alpha_T} \quad (8)$$

where A_{13} is the normalization at $10^{13} h^{-1} M_\odot$ in units of 10^{-6} and α_{M_g} is the slope of the SZE- M_g relation. Similarly, A_5 is the normalization at 5 keV in units of 10^{-5} and α_T is the slope of the SZE- T_m relation. Table 2-4 list the best-fit normalizations and slopes measured at different radii for a $z=0$ sample. The errorbars indicate a 2σ confidence region of the best-fit slope and normalization in the CSF runs at each epoch.

Fig. 7 shows that both the SZE- M_g and the SZE- T_m relations are as equally tight as the SZE-M relation. The best-fit slopes of the AD runs are in a very good agree-

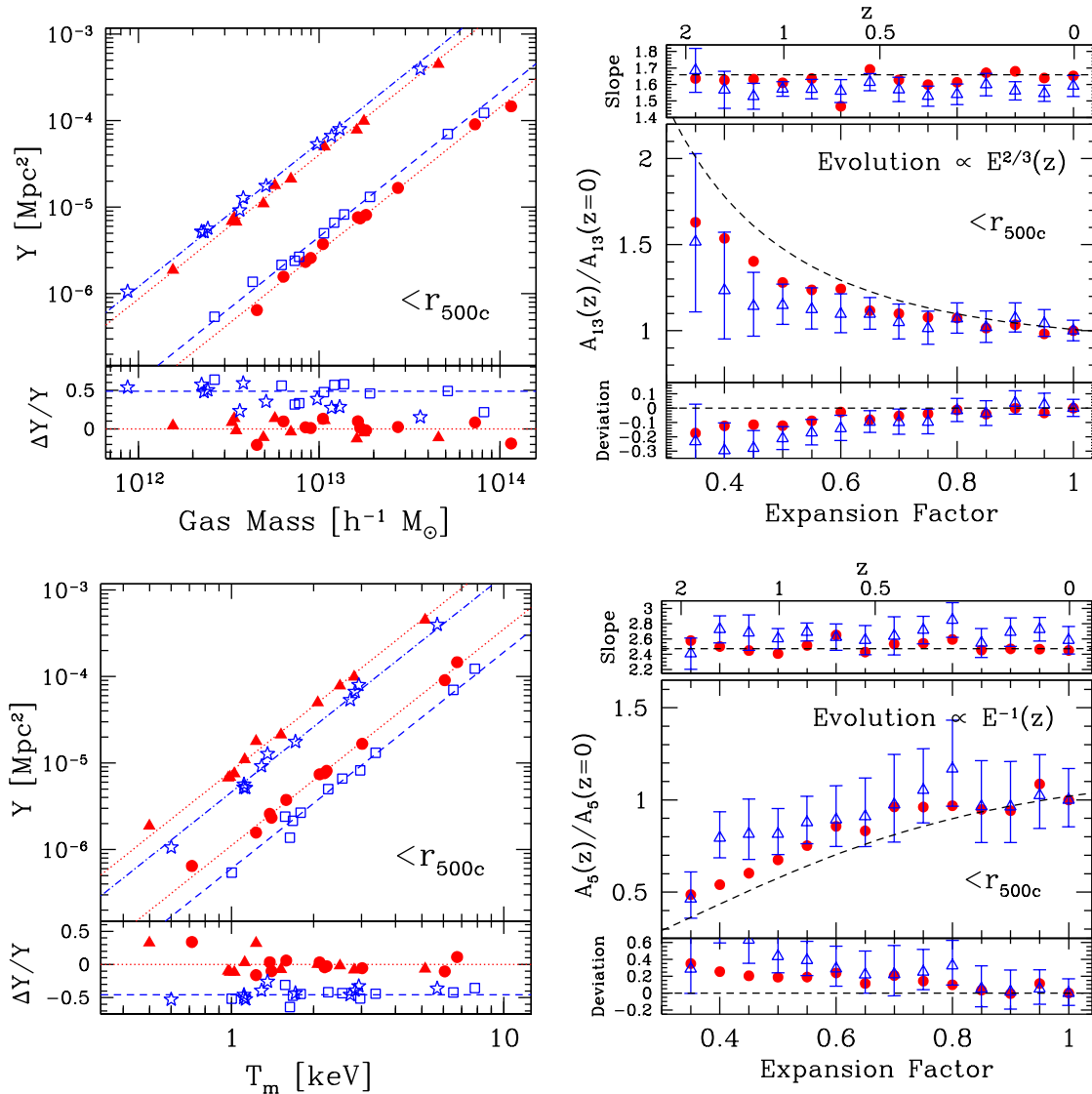


FIG. 7.— *Top panels:* the SZE flux-gas mass relations. The *left panel* shows the scaling relations at $z=0$ (*bottom lines and points*) and 1 (*top lines and points*). The *right panel* shows the redshift evolution in slope and normalization between $z=2$ and 0. The errorbars indicate 2σ confidence region of the best-fit slope and normalization in the CSF runs at each epoch. Point and line types are the same as in Fig. 3. *Bottom panels:* the relation between the SZE flux and the mass-weighted temperature.

ment with the self-similar slope. The best-fit slopes of the CSF runs, on the other hand, are marginally consistent with the predicted slope, and there are indications that the slopes in the CSF run may be slightly smaller (larger) for the SZE- M_g (SZE- T_m) relations. We also find that the slope is constant with time in both the AD and CSF runs.

Existence of tight relations between the SZE observable and cluster masses and temperature is encouraging news for future cosmological studies. In fact, the tightness of these relations is rather remarkable, because the samples analyzed here include clusters in a wide range of dynamical states. This indicates that the integrated thermal SZE signal is not very sensitive to dynamical states of clusters, making the thermal SZE an excellent proxy of cluster mass. The reason that the thermal SZE works so well is as follows. Fundamentally, the ICM is trapped in the external potential of the dark matter and

the gas must remain in approximate hydrostatic equilibrium in the dark matter potential provided that the perturbations are small compared to the energy scale of the cluster itself. The pressure profile is therefore determined by approximate force balance against gravity, and the thermal SZE measures the integral of that profile.

While the tightness and slopes of these relations are relatively unaffected, gas cooling and star formation have a large impact on their normalization. Fig. 7 shows that the normalization of the CSF run is higher by 49% in the SZE- M_g relation at r_{500c} , while it is lower by 39% in the SZE- T_m relation. Note that the change in the normalization of the SZE- M_g relation has an opposite sign from the change in the SZE- M relation, because gas cooling and star formation significantly reduce cluster gas mass. Recall that the inclusion of these physical processes reduces the SZE signal by 29% and M_g by 35% at r_{500c} . For the slope of $5/3$, a decrease in M_g by 35% in the x

TABLE 2
NORMALIZATION AND SLOPE OF THE SZE-TOTAL MASS
RELATIONS AT $z=0$

Δ	A_{14}^{ad}	α_M^{ad}	A_{14}^{csf}	α_M^{csf}
180m	$2.59^{+0.31}_{-0.28}$	1.63 ± 0.09	$1.88^{+0.18}_{-0.17}$	1.68 ± 0.07
vir	$3.11^{+0.38}_{-0.34}$	1.61 ± 0.09	$2.20^{+0.22}_{-0.20}$	1.67 ± 0.08
200c	$3.78^{+0.42}_{-0.38}$	1.62 ± 0.10	$2.56^{+0.24}_{-0.22}$	1.70 ± 0.08
500c	$4.99^{+0.46}_{-0.42}$	1.66 ± 0.09	$3.29^{+0.26}_{-0.24}$	1.73 ± 0.08
2500c	$8.82^{+0.65}_{-0.60}$	1.68 ± 0.07	$5.22^{+0.45}_{-0.41}$	1.77 ± 0.09

TABLE 3
NORMALIZATION AND SLOPE OF THE SZE-GAS MASS
RELATIONS AT $z=0$

Δ	A_{13}^{ad}	α_{Mg}^{ad}	A_{13}^{csf}	α_{Mg}^{csf}
180m	$1.55^{+0.23}_{-0.20}$	1.63 ± 0.09	$2.19^{+0.22}_{-0.20}$	1.60 ± 0.07
vir	$1.86^{+0.25}_{-0.22}$	1.61 ± 0.09	$2.61^{+0.23}_{-0.21}$	1.60 ± 0.07
200c	$2.29^{+0.22}_{-0.20}$	1.62 ± 0.07	$3.24^{+0.21}_{-0.20}$	1.60 ± 0.06
500c	$3.08^{+0.27}_{-0.25}$	1.65 ± 0.08	$4.59^{+0.28}_{-0.27}$	1.60 ± 0.06
2500c	$6.31^{+0.43}_{-0.41}$	1.64 ± 0.07	$9.27^{+0.60}_{-0.56}$	1.58 ± 0.05

direction corresponds to an increase in normalization by a factor of two. Combined with a reduction of the SZE signal, the net effect is an increase in normalization by 49% at r_{500c} . Note that the effects become larger in the inner region of the clusters. Similar accounting works for the SZE- T_m relation.

In contrast to the SZE-M relation, gas cooling and star formation modify the redshift evolution of normalization in the SZE- M_g and the SZE- T_m relations. In the CSF run, the normalization of the SZE- M_g relation is systematically lower by $\approx 20\%$ at $z=1$ than the prediction of the self-similar evolution model, while the SZE- T_m relation is higher by $\approx 40\%$ at $z=1$. The departure from the predicted evolution is mainly due to the evolution in f_{gas} and T_m , not the SZE signal, as discussed above (see also Fig. 6). Note also that the redshift evolution of the AD simulations is consistent with the self-similar model at all redshift.

4.3. Comparisons to Previous Work

We now compare the results of our simulations to previous studies in literature (White et al. 2002; da Silva et al. 2004; Motl et al. 2005). So far, all of the previous studies have focused on simulating a large number of clusters. While these simulations provide good statistics, the resolution is inevitably limited to capture relevant physical processes. The present work is on the

TABLE 4
NORMALIZATION AND SLOPE OF THE SZE-TEMPERATURE
RELATIONS AT $z=0$

Δ	A_5^{ad}	α_T^{ad}	A_5^{csf}	α_T^{csf}
180m	$18.24^{+4.65}_{-3.71}$	2.52 ± 0.18	$12.06^{+3.43}_{-2.67}$	2.60 ± 0.21
vir	$14.11^{+2.80}_{-2.34}$	2.52 ± 0.15	$9.18^{+2.04}_{-1.67}$	2.63 ± 0.19
200c	$9.98^{+1.33}_{-1.34}$	2.50 ± 0.13	$6.37^{+1.17}_{-0.99}$	2.62 ± 0.17
500c	$5.97^{+0.84}_{-0.74}$	2.45 ± 0.12	$3.63^{+0.62}_{-0.53}$	2.61 ± 0.17
2500c	$2.10^{+0.37}_{-0.32}$	2.50 ± 0.17	$1.19^{+0.18}_{-0.16}$	2.73 ± 0.19

other end of the spectrum: the resolution is high, but the statistic is low. In this sense, our work is complimentary to the previous studies.

Using SPH simulations, da Silva et al. (2004) studied the SZE scaling relations in adiabatic simulations and re-simulations in which gas was allowed to cool or was pre-heated. These studies showed that both strong gas cooling and preheating modify the slope of the SZE-M relation. They find that the slope in their cooling run ($\alpha_M = 1.79$) was steeper than the slope of their adiabatic run ($\alpha_M = 1.69$) by about 0.1. More recently, Motl et al. (2005) used a large sample of clusters simulated using an Eulerian AMR code and studied the SZE-M relation in the adiabatic run and three resimulations in which they added gas cooling, star formation and feedback one at a time. These studies showed that the slope in the simulations that include both gas cooling and star formation is very similar to the slope of the adiabatic run. Similar results are obtained using simulations performed with the entropy conserving Gadget code with cooling, star formation and feedback (White et al. 2002). Results of our simulations are also consistent with these findings. Moreover, Motl et al. (2005) showed that the slope in the cooling only run is steeper than the slope in the adiabatic run by about 0.1, consistent with results reported by da Silva et al. (2004).

In addition, da Silva et al. (2004) investigated the redshift evolution of the slope and scatter. They showed that the slope and normalization of the SZE-M relation evolve with redshift according to the self-similar model out to $z=2$ in their adiabatic and cooling only runs. Motl et al. (2005) also found similar results in all four sets of their simulations up to $z=1.5$. We reached the same conclusions using our high-resolution simulations.

In summary, the scatter, slope and redshift evolution of the SZE observable-mass relation are generally insensitive to details of cluster gas physics. These results appear to be very robust. In fact, the agreement among different studies is rather remarkable, because these simulations were carried out using very different numerical techniques, resolution and implementation of various physical processes incorporated in simulations.

Despite the robustness of the results discussed so far, the impact of galaxy formation on normalization of the SZE scaling relations is not yet well understood, because the effect is closely related to the cold baryon fractions, which have not yet converged among different simulations. da Silva et al. (2004), for example, find that

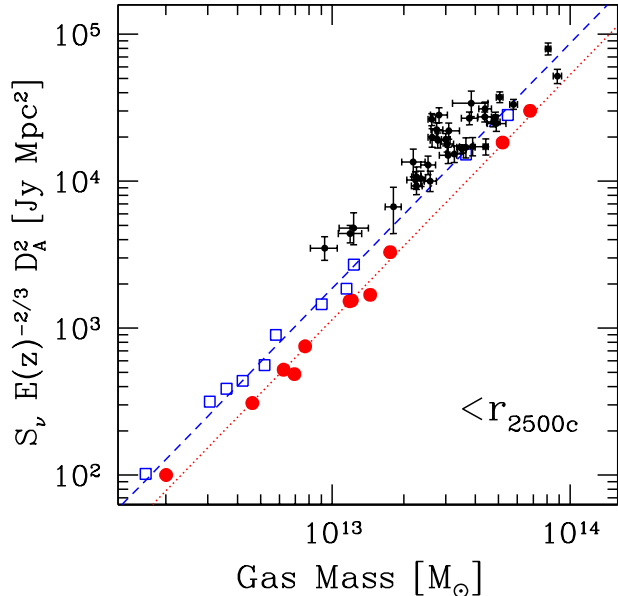


FIG. 8.— Comparisons of the SZ flux-gas mass relations in the simulations and observations. The *data points with errorbars* show the BIMA/OVRO SZ+Chandra X-ray cluster observations for a sample of 36 clusters (LaRoque 2005). The SZ flux is the integrated flux within the 2D projected aperture of R_{2500c} , while the gas mass is the enclosed gas mass within the sphere of r_{2500c} . The SZ flux is also corrected for the redshift evolution assuming the self-similar evolution model and the Λ CDM cosmology. The *solid circles* and *open triangles* show the eleven simulated clusters in the adiabatic and cooling and star formation runs, respectively, at $z=0$. The *dotted* and *dashed* lines are the best-fit relations at $z=0$ of each set of simulation. The figure shows that the simulations that include gas cooling and star formation are in reasonably good agreement with the data, while the adiabatic simulations are inconsistent with the observed relation.

the normalization of the SZE-M relation in their cooling only run is lower by 20% and 9% at $M_{200c} = 10^{14}$ and $5 \times 10^{14} h^{-1} M_{\odot}$ compared to the adiabatic run, respectively. Moreover, White et al. (2002) find even smaller effects in their simulation, because of the efficient energy feedback model used to regulate conversion of hot gas into stars (Springel & Hernquist 2002). Using our high-resolution simulations, we report that processes of galaxy formation lower the normalization of the SZE-M relation by 41, 34 and 32% at r_{2500c} , r_{500c} and r_{200c} , respectively, almost uniformly throughout the cluster mass range. This is one of the largest impact of galaxy formation on the SZE scaling relations reported to date.

4.4. Comparisons to Observations

To gauge how well the current simulations compare to data, we compare the scaling relations in our simulations to recent observational results. Figure 8 shows a comparison of the SZE flux-gas mass relation from our simulations to recent observational results based on a sample of 36 clusters between $z=0.14$ and $z=0.89$, observed with the SZE BIMA/OVRO interferometers and *Chandra* X-ray telescope (LaRoque 2005). For comparison, we use the SZE flux-gas mass relation, rather than the SZE-total mass relation, because gas mass can be measured more accurately using *Chandra* X-ray observations (see LaRoque 2005). The SZE flux is an integrated flux

within a 2D projected aperture of R_{2500c} , while the gas mass is the enclosed gas mass within a sphere of r_{2500c} . These quantities are computed using the best-fit parameters of the isothermal β model, fit jointly to the SZE and the *Chandra* data (see LaRoque 2005, for details). The observed SZE flux at a given redshift is also corrected for the redshift evolution assuming the canonical self-similar model and the Λ CDM cosmology.

In the simulations, the SZE flux is computed by projecting a sphere of $3 \times r_{500c}$ centered around the minimum of a cluster potential. Note that hot gas in the cluster outskirts makes non-negligible contribution to the integrated SZE signal, if the projected aperture is a small fraction of the cluster virial radius. For a projected radius of R_{2500c} , approximately 35% of the SZE signal arises from a region outside a sphere of r_{2500c} , on average. The projection effect varies by about 20% among different clusters, but we did not find systematic variation of the effect with cluster mass. The contribution of the cluster outskirts becomes less significant as we make the projected aperture larger. The projection of the hot gas associated with dense structures in the foreground or background of the cluster is not accounted for in this comparison.

The comparison shows that the adiabatic simulations are strongly inconsistent with data. Inclusion of gas cooling and star formation brings simulations in a better agreement with observations. However, a discrepancy between simulations and observations still remains. More specifically, there are indications that the normalization is larger, and the slope is shallower for the observed relation (see LaRoque 2005). However, the remaining discrepancy is at a level of systematic uncertainties in current measurements (see e.g., Benson et al. 2004). It is therefore critical to resolve systematic uncertainties among different instruments and to increase the cluster sample especially at low-masses to provide a better leverage on the slope of the relations.

5. DISCUSSION & CONCLUSIONS

We have presented the analysis of the Sunyaev-Zel'dovich effect (SZE) scaling relations using high-resolution simulations of galaxy clusters formed in a concordance Λ CDM cosmology. The simulations of eleven individual clusters spanning a decade in mass ($M_{500c} = 3.5 \times 10^{13}$ to $9 \times 10^{14} h^{-1} M_{\odot}$) are performed with the shock-capturing Eulerian adaptive mesh refinement N-body+gasdynamics ART code. We study the effects of gas cooling and star formation on the SZE scaling relations and their redshift evolution between $z=0$ and $z=2$ by comparing two sets of simulations performed with and without these processes included. The main results are summarized as follows.

1. The SZE signal integrated to a sufficiently large fraction of cluster volume correlates very strongly with the enclosed total cluster mass, independent of details of gas physics and dynamical state of clusters. The rms scatter of the SZE-total mass relation is about 10-15%.
2. The slope of the relation in the adiabatic run is in a very good agreement with the predicted slope of the self-similar model in the entire redshift range.

We find that the impact of galaxy formation on the slope is small ($\lesssim 0.1$).

3. The redshift evolution of the SZE-total mass relation is consistent with the self-similar model between $z=0$ and $z=2$: (a) the slope is constant with redshift and (b) the normalization evolves with redshift according to the self-similar evolution model.
4. Gas cooling and star formation significantly modify the normalization of the SZE flux-total mass relation. Inclusion of these physical processes causes a decrease in the normalization by 41, 34 and 27% at r_{2500c} , r_{500c} and r_{180m} , respectively. The decrease is due to a large decrease in gas fraction, which is offset somewhat by an increase in mass-weighted temperature. Gas cooling and star formation also cause an increase in total cluster mass and hence modify the normalization by a few percent.
5. The integrated SZE signal also correlates strongly with gas mass and mass-weighted temperature of clusters. The results (1)-(3) apply equally well for these relations, except that the redshift evolution of the normalization exhibits some deviations from the self-similar model, which increases toward higher redshifts. Gas cooling and star formation also significantly modify the normalization of these relations.
6. The SZE flux-gas mass relation in the simulations with gas cooling and star formation is in a better good agreement with the observed relation for a sample of 36 OVRO/BIMA SZE+*Chandra* X-ray observations (LaRoque 2005) than the simulations neglecting galaxy formation.

These results have a number of important implications for cosmological studies with upcoming SZE cluster surveys. First and foremost, the SZE fluxes of clusters exhibit a remarkable regularity at all redshifts, and the SZE signal integrated to a sufficiently large fraction of cluster volume is insensitive to merging events (see e.g., Motl et al. 2005) or properties of a cluster core (see § 4.1). This indicates that the integrated SZE flux is an extremely good proxy for cluster mass. Second, the slope and the redshift evolution of the SZE scaling relations are insensitive to details of cluster gas physics, and they are well characterized by a simple self-similar cluster model between $z=0$ and 2. The simplicity of their redshift evolution implies that the self-calibration (Hu 2003; Majumdar & Mohr 2004) will be effective. Finally, these results appear to be very robust, as the same conclusions have been reached using simulations with very different numerical techniques, resolution and implementation of various physical processes incorporated in simulations (see § 4.3).

Despite the simplicity of redshift evolution, the normalization of the SZE flux-mass relation is much less understood, because the effect is closely related to the cold baryon fraction, which has not yet converged among different simulations. Using high-resolution cluster simulations, we show that processes of galaxy formation have a significant impact on the normalization of the SZE scal-

ing relations. Gas cooling and star formation suppress the normalization by $\approx 30 - 40\%$, primarily due to a large reduction in cluster gas mass fraction. Interestingly, the SZE scaling relations in these simulations are in a reasonably good agreement with recent observations. Moreover, the gas mass fractions in these simulations compare well with measurements from deep *Chandra* X-ray observations of nearby clusters (Kravtsov et al. in preparation). Despite these successes in matching SZE and X-ray observations, the current cluster simulations may still suffer from the "overcooling" problem since the fraction of baryons in the cold gas and stars within a virial radius at $z=0$ is in a range 0.25-0.35, at least a factor of two higher than observational measurements (see Kravtsov et al. 2005, and discussions and references therein).

Given the importance of these issues, further efforts from observers and theorists are needed to better understand the SZE scaling relations for cosmological studies. Observationally, it is important to increase the sample size and the number of low-mass clusters. Comparisons of different instruments will also help resolve systematic uncertainties among different instruments (see e.g., Benson et al. 2004). It is also critical to understand systematic uncertainties in measurements of cluster mass through detailed and extensive comparisons of X-ray, SZE and optical observations. With the advent of a number of dedicated SZE survey instruments, the observational situation is expected to improve rapidly.

Theoretically, it is important to push detailed theoretical modelling of cluster formation to investigate roles of various physical processes, such as thermal conduction and AGN feedback, in shaping the properties of the ICM. For cosmological application, it is also critical to understand projection effects (White et al. 2002) and nature of scatter in observable-mass relations (Lima & Hu 2005). Numerical simulations of cluster formation will likely provide important insights into these issues and help assess the effectiveness of the self-calibration technique (Hu 2003; Majumdar & Mohr 2004) for future cluster surveys.

I would like to thank Andrey Kravtsov and John Carlstrom for their invaluable guidance and advice during the course of this Ph.D. project. I would also like to thank Sam LaRoque for many useful discussions on SZE observations and providing data points for the comparison with simulations. I also thank Gus Evrard, Wayne Hu and Clem Pryke for useful feedback on this work and the anonymous referee for many constructive comments on the manuscript. This project was supported by the NASA Graduate Student Researchers Program and by NASA LTSA grant NAG5-7986. I also acknowledge the support from the Sherman Fairchild Postdoctoral Fellowship at Caltech, where the final revision to the manuscript was made. The cosmological simulations used in this study were performed on the IBM RS/6000 SP4 system (*copper*) at the National Center for Supercomputing Applications (NCSA).

REFERENCES

- Carlstrom, J. E., Holder, G. P., & Reese, E. D. 2002, *ARA&A*, 40, 643
- Cooray, A. R. 1999, *MNRAS*, 307, 841
- da Silva, A. C., Kay, S. T., Liddle, A. R., & Thomas, P. A. 2004, *MNRAS*, 348, 1401
- Diaferio, A., Borgani, S., Moscardini, L., Murante, G., Dolag, K., Springel, V., Tormen, G., Tornatore, L., & Tozzi, P. 2005, *MNRAS*, 356, 1477
- Ferland, G. J., Korista, K. T., Verner, D. A., Ferguson, J. W., Kingdon, J. B., & Verner, E. M. 1998, *PASP*, 110, 761
- Gnedin, O. Y., Kravtsov, A. V., Klypin, A. A., & Nagai, D. 2004, *ApJ*, 616, 16
- Gonzalez, A. H., Zabludoff, A. I., & Zaritsky, D. 2005, *ApJ*, 618, 195
- Haardt, F. & Madau, P. 1996, *ApJ*, 461, 20
- Haiman, Z., Mohr, J. J., & Holder, G. P. 2001, *ApJ*, 553, 545
- Holder, G. P., Mohr, J. J., Carlstrom, J. E., Evrard, A. E., & Leitch, E. M. 2000, *ApJ*, 544, 629
- Hu, W. 2003, *Phys. Rev. D*, 67, 081304
- Jungwiert, B., Combes, F., & Palouš, J. 2001, *A&A*, 376, 85
- Kaiser, N. 1986, *MNRAS*, 222, 323
- Kennicutt, R. C. 1998, *ApJ*, 498, 541
- Klypin, A., Kravtsov, A. V., Bullock, J. S., & Primack, J. R. 2001, *ApJ*, 554, 903
- Kravtsov, A. V. 1999, PhD thesis, New Mexico State University
- Kravtsov, A. V., Klypin, A., & Hoffman, Y. 2002, *ApJ*, 571, 563
- Kravtsov, A. V., Nagai, D., & Vikhlinin, A. A. 2005, *ApJ*, 625, 588
- LaRoque, S. J., Bonamente, M., Carlstrom, J. E., Joy, M. K., Nagai, D., Reese, E. D., & Dawson, K. S. 2006, *ApJ* submitted (astro-ph/0604039)
- LaRoque, S. 2005, PhD thesis, University of Chicago
- Lima, M. & Hu, W. 2005, *Phys. Rev. D*, 72, 043006
- Lin, Y.-T. & Mohr, J. J. 2004, *ApJ*, 617, 879
- Majumdar, S. & Mohr, J. J. 2004, *ApJ*, 613, 41
- McCarthy, I. G., Babul, A., Holder, G. P., & Balogh, M. L. 2003, *ApJ*, 591, 515
- Metzler, C. A. 1998, unpublished (astro-ph/9812295)
- Miller, G. E. & Scalo, J. M. 1979, *ApJS*, 41, 513
- Motl, P. M., Hallman, E. J., Burns, J. O., & Norman, M. L. 2005, *ApJ*, 623, L63
- Nagai, D. & Kravtsov, A. V. 2005, *ApJ*, 618, 557
- Navarro, J. F., Frenk, C. S., & White, S. D. M. 1996, *ApJ*, 462, 563
- . 1997, *ApJ*, 490, 493
- Springel, V. & Hernquist, L. 2002, *MNRAS*, 333, 649
- Sunyaev, R. A. & Zeldovich, Y. B. 1970, *Comments on Astrophysics and Space Physics*, 2, 66
- . 1972, *Comments on Astrophysics and Space Physics*, 4, 173
- Verde, L., Haiman, Z., & Spergel, D. N. 2002, *ApJ*, 581, 5
- Vikhlinin, A., Kravtsov, A., Forman, W., Jones, C., Markevitch, M., Murray, S. S., & Van Speybroeck, L. 2006, *ApJ*, 640, 691
- Vikhlinin, A., Markevitch, M., Murray, S. S., Jones, C., Forman, W., & Van Speybroeck, L. 2005, *ApJ*, 628, 655
- Voit, G. M. 2005, *Rev.Mod.Phys.*, 77, 207
- Voit, G. M. & Bryan, G. L. 2001, *Nature*, 414, 425
- Wang, L. & Steinhardt, P. J. 1998, *ApJ*, 508, 483
- Weller, J., Battye, R. A., & Kneissl, R. 2002, *Physical Review Letters*, 88, 231301
- White, M., Hernquist, L., & Springel, V. 2002, *ApJ*, 579, 16
- Woosley, S. E. & Weaver, T. A. 1995, *ApJS*, 101, 181